Innovative microchannel-structured beads for microscale process intensification: A case study on water treatment for sulfamethoxazole abatement

Jiaojiao Zheng [a], Zhentao Wu [a,*]

[a] *Energy and Bioproducts Research Institute (EBRI), Aston University, Birmingham B4 7ET, UK*

ARTICLE INFO

ABSTRACT

This study focuses on the development of innovative microchannel-structured beads, designed to revolutionize diffusional mass transfer inside porous materials. Specifically, we created microchannel-structured alumina beads (AS0, 3 mm in diameter), using a combined phase-inversion and sintering process. This was followed by incorporating varying amounts of mesoporous γ-Al$_2$O$_3$ phase through a sol–gel process for the first time to enhance the internal specific surface area (S$_{BET}$) of the AS0 beads, along with a 2 wt% cobalt catalytic phase applied via impregnation (2Co/ASx). A second approach for integrating cobalt-γ-Al$_2$O$_3$ inside the beads is a one-step co-impregnation process (2Co/ASx (co-imp.), x ranges from 0 to 4 with varying amounts of γ-Al$_2$O$_3$ sols). These samples were then subjected to the degradation of sulfamethoxazole (SMX) in the peroxymonosulfate (PMS)-activated AOPs system under mild reaction conditions. Experimental results demonstrated that the microchannel-structured beads with higher S$_{BET}$ displayed enhanced catalytic activity, with 2Co/ASx (co-imp.) achieving better catalytic efficiency compared to 2Co/ASx. This improvement was attributed to larger exposed open surface pores on the beads, which facilitated diffusional mass transfer of reactants and products. However, overloading γ-Al$_2$O$_3$ could reduce the accessibility of surface pores, increase mass transfer resistance at high pollutant concentrations (40 mg/L SMX), and consequently reduce SMX removal efficiency. More importantly, it is unexpected that the catalyst exhibited substantially higher performance after regeneration, achieving 96.32 % SMX removal in 20 min, compared to 95.75 % in 120 min for the fresh catalyst. This was attributed to the enhanced accessibility of open pores on the bead surface during regeneration, highlighting the significance of intensifying the diffusional transfer process to benefit catalytic reactions. Such benefits are highly transferable to a broader spectrum of heterogeneous catalysis applications.

1. Introduction

Process intensification (PI), introduced by Ramshaw nearly three decades ago, is a strategy in chemical engineering aimed at making dramatical reductions in the size and complexity of chemical processes, while simultaneously achieving a substantially smaller, cleaner, safer and more energy efficient technology [1]. It entails the design of novel process-intensifying equipment and processing methods of increased volumetric productivity but reduced energy consumption, without compromising process safety and product quality. In such systems, the speed of some process, e.g., reaction kinetics, may be increased due to the reduction of physical dimensions and transport limitations [2]. Interesting applications involve chip-based microreactors [3],

multiphase microreactors [4], microchannel reactors [5], ceramic foam supports [6], and monolithic substrates [7], etc. These designed microchannel structures with lateral dimensions ranging from 0.01 to 1 mm [8], technically provide shorter diffusional paths compared to conventional reactor designs. However, catalysts within this size range typically cause a high pressure drop in packed bed reactors. As a result, the industry tends to employ relatively larger catalysts, ranging from 1-3 mm in diameter [9]. This, in turn, results in more severe mass transfer resistance inside the catalyst, especially when catalyst and/or catalyst support sizes surpass 300 μm [10].

A case in point, conventional monolithic substrates feature numerous straight, thin-walled narrow parallel channels to improve the mass transfer effectiveness [7,11]. The greater number of channels, namely

higher cells per square inch (CPSI), reduces diffusion resistance within the catalytic layer, leading to enhanced reaction activity. However, a further increase of CPSI, such as reaching 900 for conventional monolithic catalytic converter, led to a sharp rise in pressure drop, therefore only monolithic substrates of 400 CPSI and 600 CPSI have been applied in automotive industry [12,13]. Mahyon et al. reported a novel hollow fibre substrate with radial microchannels (900 CPSI), which could reduce the diffusional resistance inside catalytic layers but maintain a low pressure drop [14]. After wash-coating a thin layer of gamma-Al₂O₃, serving as the support for the active species (0.7 wt% Pd), on the inner walls of these microchannels, the wash-coated samples could further lower the light-off temperatures of CO oxidation at low pressure drops.

In the development of PI equipment, particularly catalyst substrates, there is a noticeable lack of innovations aimed at intensifying PI at the microscale or within the pellets. Spherical catalyst substrates featuring innovative special structures, such as shape-selective designs, optimised pore radii distributions and connectivity, might be a turning point to facilitate the reaction process [15]. Being the most commonly used catalyst support shape, spheres ensure uniform packing and provide better resistance to attrition than other shapes, achieving a relative lower pressure drop. However, the commercial catalyst supports in packed-bed reactors are typically either porous beads with isotropic structures [16,17] or eggshell pellets with a thin catalyst layer on the surface [18]. This is due to the long-standing challenges of balancing pressure drop and intraparticle diffusion resistance, as previously described.

In our recent research, we developed a novel microchannel-structured alumina beads (3 mm) with radial straight finger-like microchannels (20–100 μm in width) inside to decouple structural limitations of current catalyst design, i.e., trade-off between diffusional mass transfer and pressure drop of packed bed units [10]. These unique beads can maintain a low pressure drop within a reactor while simultaneously provide high geometrical surface areas. For any sphere beads, the simplest textual model for the effective diffusion coefficient ($D_{e,i}$) derived from the molecular diffusion coefficient (D_i), the average porosity (ε_p) and tortuosity (τ_p) of the material [19]:

$$D_{e,i} = \frac{\varepsilon_p}{\tau_p} D_i \tag{1}$$

At a fixed particle porosity, the effective diffusion coefficient is inversely proportional to tortuosity. Therefore, the tradeoff between tortuosity and geometrical surface area in conventional uniform beads makes it difficult to sustain a high value of $D_{e,i}$. In contrast, microchannel-structured alumina beads possess shorter transport distances and lower tortuosity due to the presence of finger-like microstructures, resulting in a significantly higher $D_{e,i}$ compared to conventional beads. It is worth noting that these beads were engineered for industrial use, with consideration given to the mechanical strength of materials, so α-Al₂O₃ was chosen other than γ-Al₂O₃ despite its relatively higher specific surface area. Generally, the weak mechanical strength of γ-Al₂O₃ can lead to rapid crumbling under intense loading. This produces dust and fragments that obstruct the spaces between pellets, resulting in a premature increase in bed pressure drop [20]. However, due to the inherent small specific surface area of α-Al₂O₃, modifications are required to enhance its catalytic performance.

γ-Al₂O₃ is one of the most used washcoating mesoporous materials. It can be prepared by the sol–gel method, which allows for uniform distribution after drying and sintering, and has been widely applied to enhance the specific surface area of the catalyst substrates [14,21]. Therefore, γ-Al₂O₃ was chosen to washcoat onto the surface of the finger-like microchannels within the innovative alumina beads (AS0) in this work to fulfil its potential for catalytic reactions. The structural advantages of these modified alumina beads were validated in a peroxymonosulfate (PMS)-activated advanced oxidation processes (AOPs) reaction system for the degradation of sulfamethoxazole (SMX) under mild reaction conditions. In contrast to conventional AOPs, persulfate-

based AOPs, including those using PMS and peroxydisulfate (PDS), can promote the generation of reactive free radicals, such as $SO_4^{·-}$, with high standard redox potentials (2.5–3.1 V vs. NHE) and long half-life time (30–40 μs) [22]. It was reported that mechanochemistry was an attractive technology for enhancing the catalytic performance of functionalised materials towards PMS activation, because mechanical energy could induce defects and destabilised the symmetry of chemical bonds [23,24]. This study introduces another promising technique, i.e., modified microchannel-structured alumina beads, for the improvement of catalytic efficiency for SMX degradation. The distinctive finger-like microstructures within the beads were originally created in our recent work [10], and in this study, these AS0 beads were modified with γ-Al₂O₃ sols, and evaluated for the first time. To the best of our knowledge, studies on microchannel-structured alumina beads of millimetre-range, i.e., AS0, are scarce. As noted, these AS0 beads feature microchannels that alleviate the constraints typically associated with catalyst substrate design, providing a shorter transport distance for catalytic reactions. This is in stark contrast to traditional homogeneous distribution of catalysts on the porous beads or the eggshell-type beads, where catalyst is confined to the surface of inert beads [16,18].

In short, the increased specific surface area of ASx samples in this study provide more accessible active sites for diffusion-limited catalytic reactions. Two different catalyst incorporation methods, i.e., two-step (2Co/ASx) and one-step (2Co/ASx (co-imp.)) approaches, were investigated and the prepared samples were systematically characterised by a series of techniques, such as BET, SEM, XPS, etc. The combined structural benefits of the novel finger-like microchannels within the alumina beads, along with an enhanced BET surface area, were expected to facilitate the catalytic efficiency of SMX elimination in a PMS-activated AOPs reaction system. Furthermore, the stability and reusability of samples were discussed to better meet with the industrial requirements. Finally, the active species involved in the 2Co/AS4|PMS reaction system were analysed through quenching experiment, and the catalytic mechanism of this reaction system was further proposed.

2. Materials and methods

2.1. Materials

In this work, cobalt nitrate hexahydrate (Co (NO₃)₂·6H₂O, 99 %), methanol (HPLC grade, ≥ 99.8 %), and nitric acid (HNO₃, analytical reagent grade, 70 %) were purchased from Fisher Scientific. Aluminium isopropoxide (AIP), Oxone® (PMS, KHSO₅·0.5KHSO₄·0.5K₂SO₄), sulfamethoxazole (SMX), p-benzoquinone (p-BQ, ≥ 98 %), *tert*-butanol (tBA, ≥99.5 %), sodium azide (NaN₃, ≥99.5 %), and acetic acid (ReagentPlus®, ≥ 99 %) were all obtained from Sigma-Aldrich. All chemicals were used as received without any further purification. Milli-Q water (18.3 MΩ cm at 25 ℃, Milli-Q® Advantage A10®) was used during the whole experimental process.

2.2. Preparation of γ-Al₂O₃-washcoated alumina beads (ASx)

Microchannel-structured alumina beads of 3 mm in diameter were prepared by a phase-inversion and sintering-assisted method, as reported in our previous work [10]. After that, a sol–gel method [25] was used to prepare γ-Al₂O₃-washcoated alumina beads. Initially, 11.34 g of aluminium precursor (AIP) was dissolved in 100 g of DI water to give a 1 M aqueous solution, and then a small amount of HNO₃ was added to the solution to maintain the pH of the suspension ~ 3.5. The suspension was refluxed and stirred vigorously at 85 ℃ for several hours until it transformed into a clear sol. The sol was then allowed to cool down to room temperature in preparation for wash-coating, where four different γ-Al₂O₃ sols were obtained by drying the cooled sol in an oven at 35 ℃ for 0 h, 8 h, 23 h, and 31 h, designated as sol 1, sol 2, sol 3, and sol 4, respectively, as per the aging time. The as-prepared sol was subsequently incorporated into the alumina beads (AS0) by immersing the

beads into the sol under vacuum for 20 min. This degassing process would facilitate the infiltration of the sol onto the inner surface of micro-channels inside. Finally, the sol–gel γ-Al₂O₃ coated specimens were sintered at 500 ℃ in a muffle furnace for 1 h. For simplicity, the speci-mens were denoted as AS1, AS2, AS3 and AS4, respectively. The increased amount of γ-Al₂O₃ sol coatings for each sample and surface area increment were summarised in Table 1.

2.3. Incorporation of Co-based catalysts (Co/ASx)

Cobalt oxide was incorporated throughout the beads by the incipient wetness impregnation method. Firstly, 0.74 g of cobalt nitrate hexahy-drate was dissolved in 4.5 mL of DI water, and then added to 10 g of ASx beads, resulting in a Co₃O₄ to alumina bead weight ratio of 2 wt%. Then, the catalyst precursor was dried and sintered at 450 ℃ for 3 h at heating and cooling rates of 5 ℃/min, as shown in Fig. 1. These catalysts were denoted as 2Co/ASx, where "x" refers to the γ-Al₂O₃ sol, as previously illustrated. In comparison, one-step co-impregnation method was applied to prepare samples 2Co/ASx (co-imp.). Specifically, after the preparation of γ-Al₂O₃ sol, 0.74 g of cobalt nitrate hexahydrate was mixed in 4 mL of γ-Al₂O₃ sols, and then 10 g of alumina beads (AS0) was added into the sols, being degassed under the vacuum for 20 min. Finally, the dried 2Co/ASx (co-imp.) was sintered at 450 ℃ for 3 h. Rather than washcoating alumina beads in the prepared γ-Al₂O₃ sol, sintering, and then incorporating with cobalt precursors, this method could attach the entire catalyst onto the microchannel walls in one step.

2.4. Characterisation

Powder X-ray diffraction (XRD) patterns of ASx and 2Co/ASx were recorded on an advanced X-ray diffractometer (Bruker D8, Germany), with Cu Kα radiation (λ = 1.5418 Å), operated at 40 kV and 40 mA. The specific surface area of samples was obtained at −196 ℃ with liquid nitrogen on a Nova 4000 porosimeter, using the Brunauer–Emmett–-Teller (BET) method and the Barrett, Joyner, and Halenda (BJH) method. Prior to the measurement, samples were gently ramped to 130 ℃ and degassed under vacuum for 5–6 h. The chemical states and compositions of samples were analysed by X-ray photoelectron spec-troscopy (XPS, Thermo Scientific K-Alpha Photoelectron spectrometer, USA) using an Al Kα source. All binding energies were calibrated by C 1 s (284.8 eV). The morphology of alumina beads, before and after cobalt loading, was analysed by a scanning electron microscopy (SEM, JEOL JSM-IT200, operating at 5 kV and working distance of 10 mm). The cobalt content was analysed by an ICP-OES apparatus (iCAP 7000 Series).

2.5. Catalytic degradation of SMX in a PMS-activated system

The catalytic performance of 2Co/ASx and 2Co/ASx (co-imp.) was evaluated for the degradation of SMX solutions in a PMS activated sys-tem. The experiments were carried out in a batch reactor in a water bath and connected with a mechanical overhead stirrer. Initially, 0.02 g of catalyst was placed in 100 mL of SMX solution with vigorously stirring at

150 rpm for 30 min to achieve the adsorption–desorption equilibrium. Afterwards, the catalytic reactions were triggered by adding PMS (0.31 mM) and continued for another 120 min. It is noteworthy that oxidant to pollutant molar ratio for 10, 20, and 40 mg/L SMX was 8.24, 4.12, and 2.06, respectively. When the reaction was in process, 1 mL of aqueous solution was withdrawn by a syringe at fixed time intervals and filtered by a 0.2 μm PTFE syringe filter, and then immediately injected into a HPLC vial which was already injected with 0.5 mL methanol as a quenching agent. The concentrations of SMX solutions were analysed on an ultra-high performance liquid chromatography (UHPLC, Shimadzu Prominence, Japan) equipped with a C-18 column (Restek Rapter, 2.7 μm, 100 × 2.1 mm, France). The target SMX pollutant was detected using a UV detector set at 270 nm of wavelength. Methanol and ultra-pure water (pH 3.5 adjusted by acetic acid) with a volume ratio of 90:10 was used as the mobile phase at a flowrate of 0.3 mL/min. The catalytic degradation kinetics of SMX followed the pseudo-first-order kinetic model and can be estimated using the following equation:

$$\ln\left(\frac{C}{C_0}\right) = -kt \tag{2}$$

where k is the apparent reaction rate constant (min⁻¹), and C_0 and C are the initial SMX concentration (mg/L), and the SMX concentration at specific time intervals (mg/L), respectively.

3. Results and discussion

3.1. Phase compositions of ASx, 2Co/ASx, and 2Co/ASx (co-imp.)

Four different γ-Al₂O₃ sol coatings were incorporated into the microchannel-structured alumina beads, and their XRD patterns in Fig. S1 demonstrated that all diffraction peaks of samples before and after cobalt impregnation were well matched with the rhombohedral phase of α-Al₂O₃ referenced in JCPD file no. 88–0826 [26]. There are no characteristic peaks of γ-Al₂O₃ observed due to the low intensity of γ-Al₂O₃ phase compared to α-Al₂O₃. A slight shift of three main char-acteristic peak positions (Fig. S1 (b) and (c)) for ASx samples might be linked to the presence of γ-Al₂O₃ [27]. No characteristic peaks of Co₃O₄ were detected in either 2Co/ASx or 2Co/ASx (co-imp.) samples, which can be ascribed to the low concentration and high dispersion of cobalt oxide. This aligns with our previous research [10] and will be further examined by the XPS result (Fig. 3 (b)), ICP results (1.77 wt% of Co for 2Co/AS4 and 1.74 wt% of Co for 2Co/AS4 (co-imp.)), and BET results (Table 2).

Table 2 summarises the textual properties of γ-Al₂O₃ sol gel-washcoated alumina beads before and after cobalt impregnation using N₂ adsorption. By adding different γ-Al₂O₃ sols into the microchannel-structured alumina beads AS0, the surface areas of ASx samples gradu-ally enhanced as the aging time for γ-Al₂O₃ sol increased, facilitating the dispersion and deposition of active components [21]. More γ-Al₂O₃ washcoatings for AS4 resulted in a much higher BET surface area (36.03 m²/g), nearly 10 folds of the one without washcoating layers (AS0, 3.65 m²/g). Meanwhile, the average pore diameter dropped slightly, accordingly, indicating the successful incorporation of γ-Al₂O₃. BET analysis of γ-Al₂O₃ powder synthesised by the sol gel method was also include for comparison, which possessed similar S_{BET} and D_p to the literature [28].

After cobalt deposition, four samples prepared using the two-step method (2Co/ASx) experienced a slight reduction in surface area, whereas the four samples prepared by the one-step method (2Co/ASx (co-imp.)) displayed a similar surface area (~10 m²/g) for samples 2Co/AS1-3 (co-imp.). As for the highest surface areas for each method, 2Co/AS4 (co-imp.) (14.47 m²/g) showed a lower value than 2Co/AS4 (21.05 m²/g). This might be attributed to two possible reasons. On the one hand, the different thermal treatment methods for 2Co/ASx and 2Co/ASx (co-imp.) might result in different material properties. In this work,
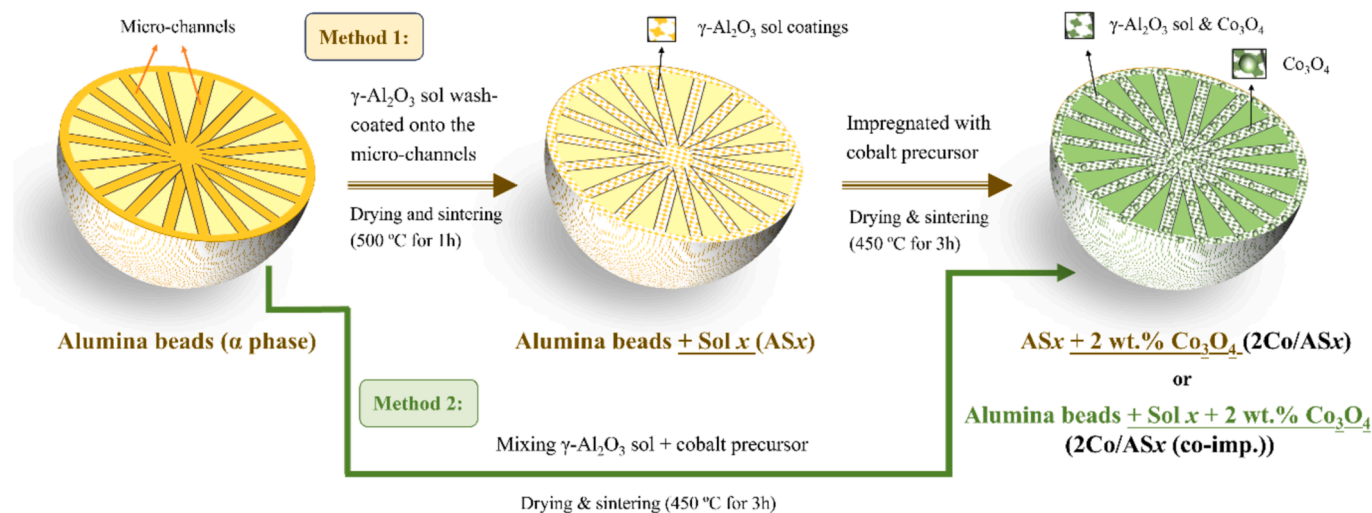
Table 1
Weight increase and specific surface area increment of γ-Al₂ O₃ wash-coated samples.

Sample	γ-Al₂O₃ sol aging time (h)	Mass before wash-coating (g)	Mass after wash-coating (g)	Wash-coated γ-Al₂O₃ (g)	γ-Al₂O₃ mass fraction (%)	Surface area increment fraction (%)
AS1	0	5.0107	5.1054	0.0947	1.90	72.5
AS2	8.5	5.0075	5.1712	0.1637	3.27	159.7
AS3	23	5.0089	5.2536	0.2447	4.89	363.7
AS4	31.5	5.0080	5.5049	0.4969	9.92	587.1

Fig.1. Diagrammatic representation of the γ-Al$_2$O$_3$ washcoating process and catalyst integration.

Table 2
Textural properties of γ-Al$_2$ O$_3$ sol-washcoated alumina beads before and after cobalt impregnation.

Sample	S$_{BET}$ (m^2/g)	V$_T$ (cc/g)	D$_p$ (nm)
AS0	3.65	0.01	14.82
AS1	7.49	0.02	9.45
AS2	9.40	0.02	9.97
AS3	13.98	0.03	7.55
AS4	36.03	0.05	5.78
γ-Al$_2$O$_3$ (sol–gel)	202.00	0.21	4.24
2Co/AS1	6.31	0.02	13.52
2Co/AS2	7.65	0.02	11.93
2Co/AS3	12.45	0.04	13.19
2Co/AS4	21.05	0.05	9.29
2Co/AS1 (co-imp.)	10.69	0.03	10.14
2Co/AS2 (co-imp.)	9.16	0.02	9.23
2Co/AS3 (co-imp.)	10.43	0.02	8.76
2Co/AS4 (co-imp.)	14.47	0.04	9.81

S$_{BET}$: surface area; V$_T$: Total pore volume; D$_P$: Average pore diameter.

2Co/ASx underwent two calcination processes (500 ℃ and 450 ℃ for the formation of γ-Al$_2$O$_3$ and Co$_3$O$_4$, respectively), whilst 2Co/ASx (co-imp.) experienced merely one (450 ℃). Researchers have reported that the calcination processes would lead to different specific surface area of the γ-Al$_2$O$_3$ washcoat [29,30]. However, 450 ℃ was normally used as the calcination temperature to transform Co (NO$_3$)$_2$·6H$_2$O into Co$_3$O$_4$ [28,31,32]. Further increasing the sintering temperature might result in the formation of CoAl$_2$O$_4$ due to the strong interaction between Co$_3$O$_4$ and γ-Al$_2$O$_3$ [28,33,34], as confirmed by the XRD results and colour change of Co/γ-Al$_2$O$_3$ pellets sintered at different temperatures (Fig. S2). On the other hand, when the catalytically active component, i.e. cobalt-based precursor, was mixed with the prepared γ-Al$_2$O$_3$ sol prior to the washcoating procedure, the rheological properties of the washcoated layer might be greatly influenced [29,35], affecting the specific surface areas accordingly.

XPS spectra of 2Co/AS0 and 2Co/AS4 were measured to verify the presence of Co element and the chemical state of 2Co/ASx samples. As shown in Fig. 2 (a), the XPS survey spectra confirmed the presence of elements Al, O, C and Co in both samples. The C 1 s spectra for both samples centred at 284.8 eV belong to adventitious carbon, which originated from the carbon grid during sample preparation process [36]. The Co 2p spectra revealed that cobalt existed in two chemical states (Co^{3+}, Co^{2+}) in both 2Co/AS0 and 2Co/AS4, corresponding to the compositions of Co$_3$O$_4$. Additionally, the shift of binding energy from 2Co/AS0 (780.0 eV) to 2Co/AS4 (780.3 eV) and lower intensity of Co 2p

spectrum in 2Co/AS4 could be attributed to the presence of γ-Al$_2$O$_3$, which is consistent with the BET results (Table 2) [37,38]. Likewise, the existence of γ-Al$_2$O$_3$ sol coatings in 2Co/AS4 resulted in higher intensities of the O 1 s spectrum (Fig. 2 (d)), and Al 2p spectrum (Fig. 2 (c)) as well as the disappearance of extremely weak peak centred at 75.3 eV in 2Co/AS0, which was associated with the formation of small amounts of aluminium suboxide during the cobalt impregnation process [10,39,40].

3.2. Morphology of microchannel-structured ASx before and after cobalt incorporation

SEM images of both the cross-sectional and surface views of microchannel-structured alumina beads without (AS0) and with γ-Al$_2$O$_3$ sol washcoatings (ASx) are depicted in Fig. 3. Before conducting SEM analysis, these beads were halved by a knife to expose their cross-sections. Fig. 3 (a-e) and Fig. 3 (a$_2$-e$_2$) presented the cross-section of ASx samples with radial microchannels, which consist of irregularly packed granules sized at approximately 400 nm. As the number of γ-Al$_2$O$_3$ coatings increased, the average width of radial microchannels decreased accordingly, with 85.59 μm, 81.92 μm, 74.62 μm, 56.98 μm, and 54.03 μm measured for AS0, AS1, AS2, AS3 and AS4, respectively. All measurements were performed from the half radii of the beads, i.e., the 1/4 region of the beads' diameter, to ensure consistency. Different from the loosely packed granular structures of α-Al$_2$O$_3$ at the inner surface of microchannels in AS0 (Fig. 3 (a$_2$)), γ-Al$_2$O$_3$ with a smooth and flat surface, marked by yellow dashed frames, could be observed in the enlarged SEM images of AS1-4 samples (Fig. 3 (b$_2$-e$_2$)). With further increased the loadings of γ-Al$_2$O$_3$ sol, the number of this thin coating layer gradually grew with the increase of γ-Al$_2$O$_3$ sol aging time. This aligns with the BET results aforementioned in Table 2 and SEM images of γ-Al$_2$O$_3$ powder in Fig. 3 (f, f$_2$). Furthermore, gamma-Al$_2$O$_3$ inside the microchannels did not cover and block the opening ends of oriented microchannels, and even the sample with the highest γ-Al$_2$O$_3$ sol loadings (AS4) remained unblocked.

As shown in Fig. 3 (a$_3$, a$_4$), before washcoating with γ-Al$_2$O$_3$ sol, the surface of the sample AS0 exhibited numerous small open channels, with an average pore size of 6.02 μm. The introduction of γ-Al$_2$O$_3$ did not change the pristine morphologies of alumina beads, but some open channels were partially blocked by γ-Al$_2$O$_3$ coatings. This might potentially increase the mass transport resistance when over-loaded with the γ-Al$_2$O$_3$ washcoatings. It is worth noting that there were no significant changes on the overall average pore sizes of open channels for ASx samples, although large amounts of γ-Al$_2$O$_3$ coatings could be
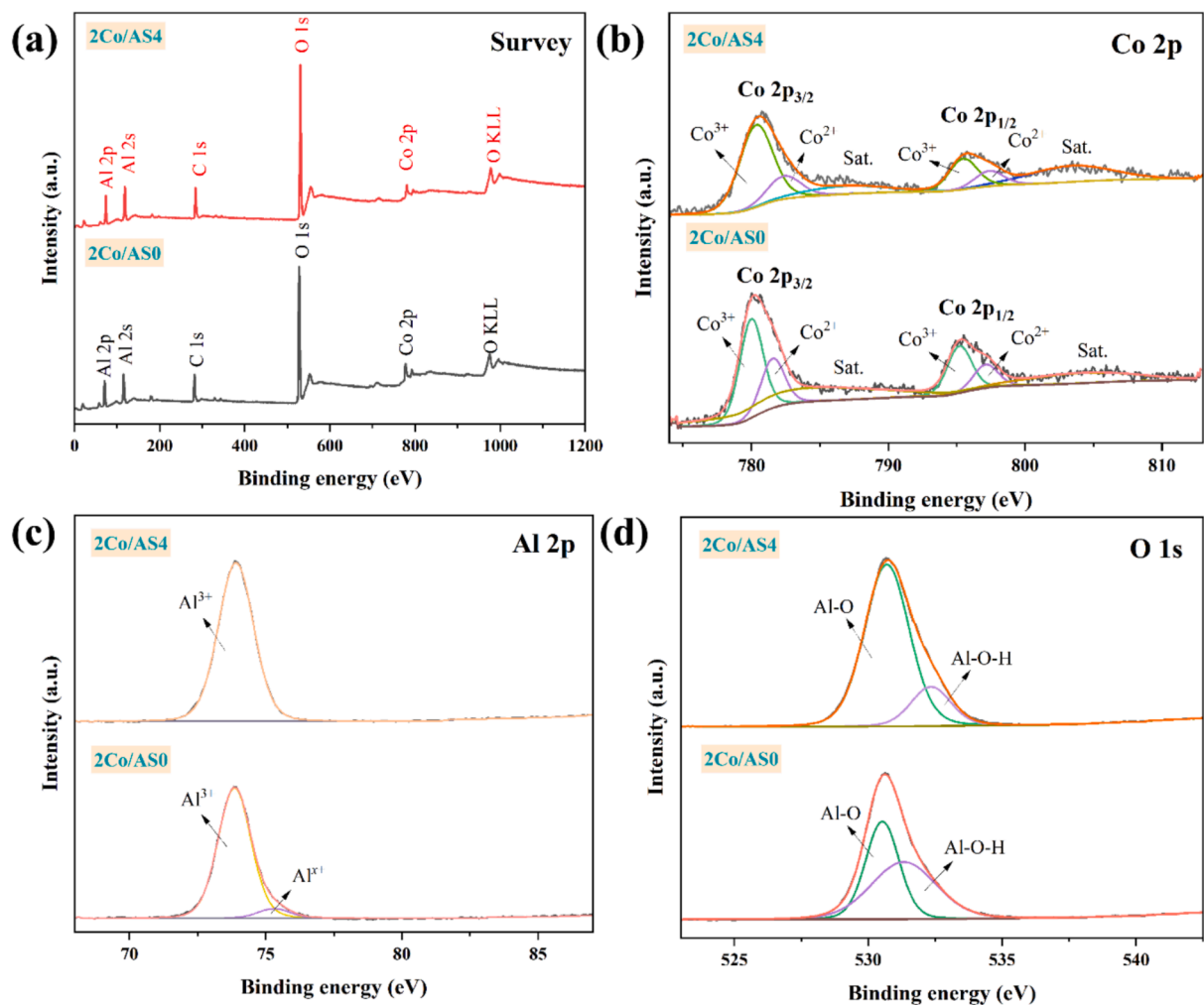
Fig.2. (a) XPS survey spectra and high-resolution XPS spectra of (b) Co 2p, (c) Al 2p and (d) O 1s of cobalt-impregnated microchannel-structured alumina beads before (2Co/AS0) and after γ-Al$_2$O$_3$ washcoating (2Co/AS4).

observed on the surface layer of AS4. In certain areas, γ-Al$_2$O$_3$ nanoparticles partially obstructed the open channels, similar to samples AS1-3, with the average pore size in these regions being 4.42 μm (Fig. 3 (e$_4$)). In contrast, γ-Al$_2$O$_3$ washcoatings accumulated into large submicron flakes in some areas, yet substantial cracks (Fig. 3 (e$_3$)) and exposed pores (Fig. 3 (f$_3$, f$_3$)) with an average size of 4.35 μm pertained.

Fig. 4 displayed the SEM images of AS4 samples after incorporating 2 wt% Co$_3$O$_4$ by two-step sequential impregnation method (2Co/AS4) and one-step co-impregnation method (2Co/AS4 (co-imp.)). Apparently, the introduction of Co$_3$O$_4$ did not alter the pristine morphologies of both alumina beads. Fig. 4 (b, b$_2$) and Fig. 4 (d, d$_2$) demonstrated that all finger-like microchannels for these two samples remained and no catalyst agglomerations could be found in the cross-section. The surface views of 2Co/AS4 in Fig. 4 (a, a$_2$, a$_3$) displayed a relative coarse texture, with an average exposed open channel size of 8.16 μm. In contrast, Fig. 4 (c, c$_2$, c$_3$) illustrated that the surface of 2Co/AS4 (co-imp.) was coated with small γ-Al$_2$O$_3$ submicron flakes, of which the sizes of flakes and exposed open channels were 20 μm and 8.01 μm, respectively. Details regarding other 2Co/AS*x* and 2Co/AS*x* (co-imp.) samples are provided in the supplementary information (Text S1, Fig. S3).

3.3. Evaluation of the catalytic performance

Based on the above characterisation results, innovative microchannel-structured alumina beads with enhanced specific surface area have been successfully prepared and cobalt-based catalysts have

been deposited on the beads. If their catalytic performance proves remarkable, it would be critically important and advantageous for microscale process intensification. The catalytic efficiency of two types of cobalt-based AS*x* samples was investigated by degrading SMX solutions (10 mg/L, 20 mg/L, 40 mg/L) at different reaction temperatures (20 ℃, 40 ℃) in a PMS-activated AOPs system, as shown in Fig. 5, Fig. 6, and Fig. S5.

Fig. 5 displays the degradation of different SMX concentrations at 20 ℃, comparing the sample before washcoating with γ-Al$_2$O$_3$ sol (2Co/AS0) to six samples that were washcoated by two different methods (2Co/AS*x* and 2Co/AS*x* (co-imp.)). The self-degradation of SMX for all reaction conditions (SMX concentrations, reaction temperatures) in this work was all negligible (< 0.1 %). As shown in Fig. 5 (a), when the initial SMX concentration was 10 mg/L, PMS alone could degrade 32.58 % of SMX, which is comparable to the research with a similar PMS dosage, i. e., either 0.31 mM, or 0.01 g/L, or an oxidant-to-pollutant molar ratio of 8.24 [41]. While the SMX removal efficiency was greatly improved using 2Co/AS0 (90.56 %). Additionally, all samples with enhanced surface area could completely remove SMX in 120 min, and 2Co/AS4 (co-imp.) could degrade 100 % SMX within 45 min. The removal efficiency for SMX in 2Co/AS*x* system witnessed a gradually increased performance as the increase of γ-Al$_2$O$_3$ sol loadings, i.e., increased specific surface area, with 2Co/AS1 (78.53 %) < 2Co/AS2 (87.01 %) < 2Co/AS3 (98.37 %) < 2Co/AS4 (100 %) within 60 min, respectively. In contrast, the catalytic activity of two 2Co/AS*x* (co-imp.) samples was also investigated, following the trend 2Co/AS2 (co-imp.) (95.01 %) < 2Co/AS4 (co-imp.)
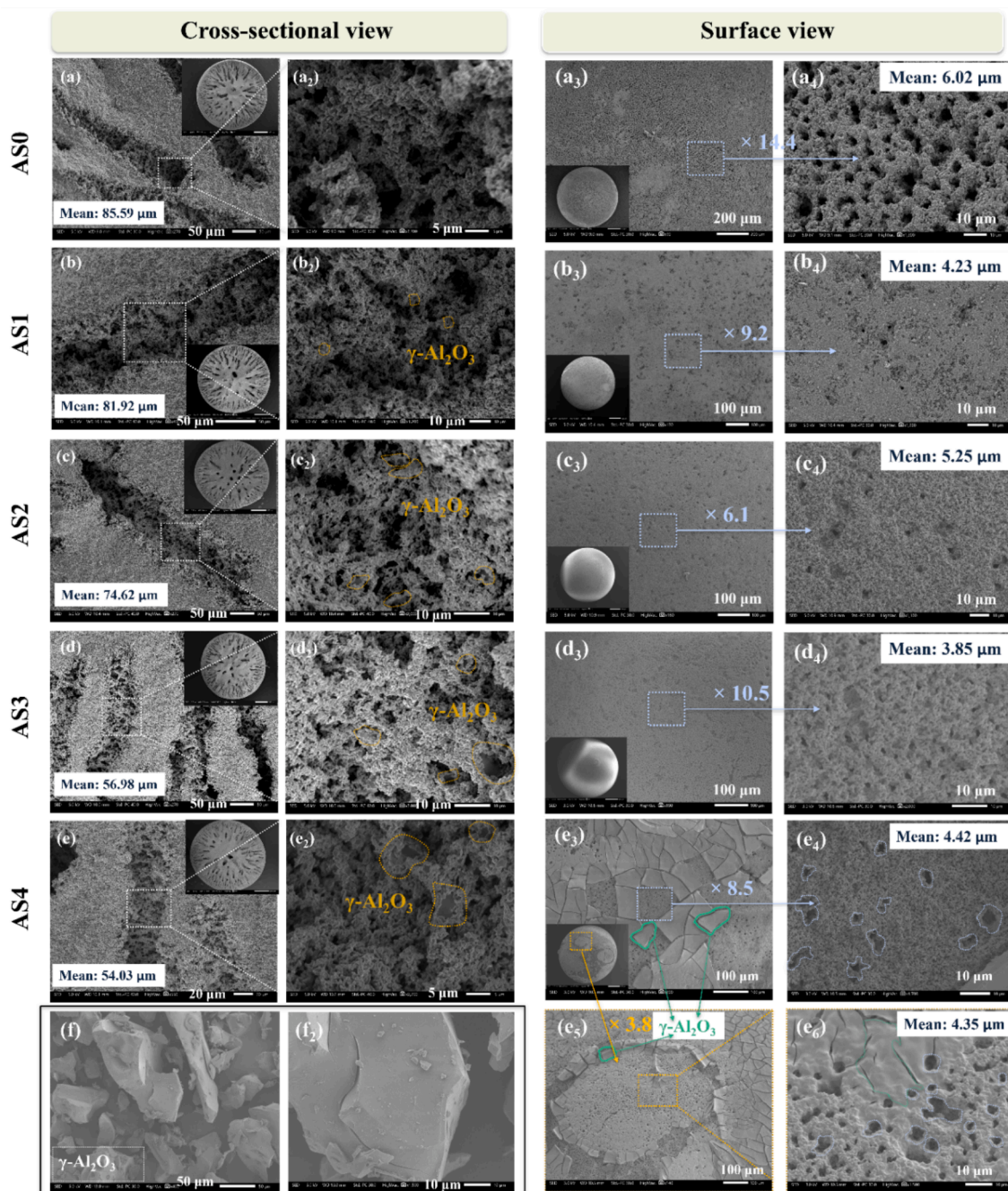
Fig.3. SEM images of the cross-sectional views of (a, a₂) micro-structured alumina beads (AS0), γ-Al₂O₃ sol-coated alumina beads (b, b₂) AS1, (c, c₂) AS2, (d, d₂) AS3, and (e, e₂) AS4; the surface views of (a₃ , a₄) AS0, (b₃ , b₄) AS1, (c₃ , c₄) AS2, (d₃ , d₄) AS3, (e₃ , e₄ , e₅ , e₆) AS4; (f, f₂) SEM images of γ-Al₂O₃ powder.

(100 %) within 60 min. Under this reaction condition, 2Co/ASx (co-imp.) samples exhibited higher catalytic performance than those in 2Co/ASx, probably due to the high dispersion of cobalt-based catalysts and larger open channel sizes on the surface, as shown in Fig. S3. Likewise, the reaction kinetics (Fig. S5 (a)) and the corresponding rate constants (Fig. 5 (b), Fig. S5 (b)) were consistent with the degradation performance. Therefore, the enhanced catalytic performance and improved utilization efficiency of volumetric productivity of 2Co/ASx and 2Co/ASx (co-imp.) samples validate the potential of these materials for the process intensification at microscale.

Moreover, when the SMX concentration increased to 20 mg/L, the degradation efficiency displayed a comparable scenario, as shown in Fig. 5 (c-d) and Fig. S5 (c-d). Nevertheless, as the SMX concentrations increased to 40 mg/L (Fig. 5 (e)), the reaction rate for 2Co/AS4 (co-imp.) was lower than 2Co/ASx samples before 120 min, which could be ascribed to the partial blockage of some regions in 2Co/ASx (co-imp.) by γ-Al₂O₃ submicron flakes (Fig. 4 (c₂)). These flakes resulted in less effective interactions between SMX molecules and active sites, thereby impeding the rapid diffusion of reactants and products, particularly at higher concentrations of organic pollutants [14]. As shown in Fig. S3 (d-f), the surfaces of samples prepared by method 2 were more easily obstructed, with the blocked regions increasing progressively from 2Co/AS1 (co-imp.) to 2Co/AS4 (co-imp.). Additionally, the disparity for SMX removal efficiency between the sample before (2Co/AS0) and after washcoating (2Co/ASx) decreased, with 59.02 %, 64.75 %, 70.14 %, 74.84 %, 74.86 %, and 75.00 % for 2Co/AS0, 2Co/AS1, 2Co/AS2, 2Co/AS3, 2Co/AS4, and 2Co/AS4 (co-imp.), respectively. This indicated that there is a balance between the BET surface area and the intraparticle
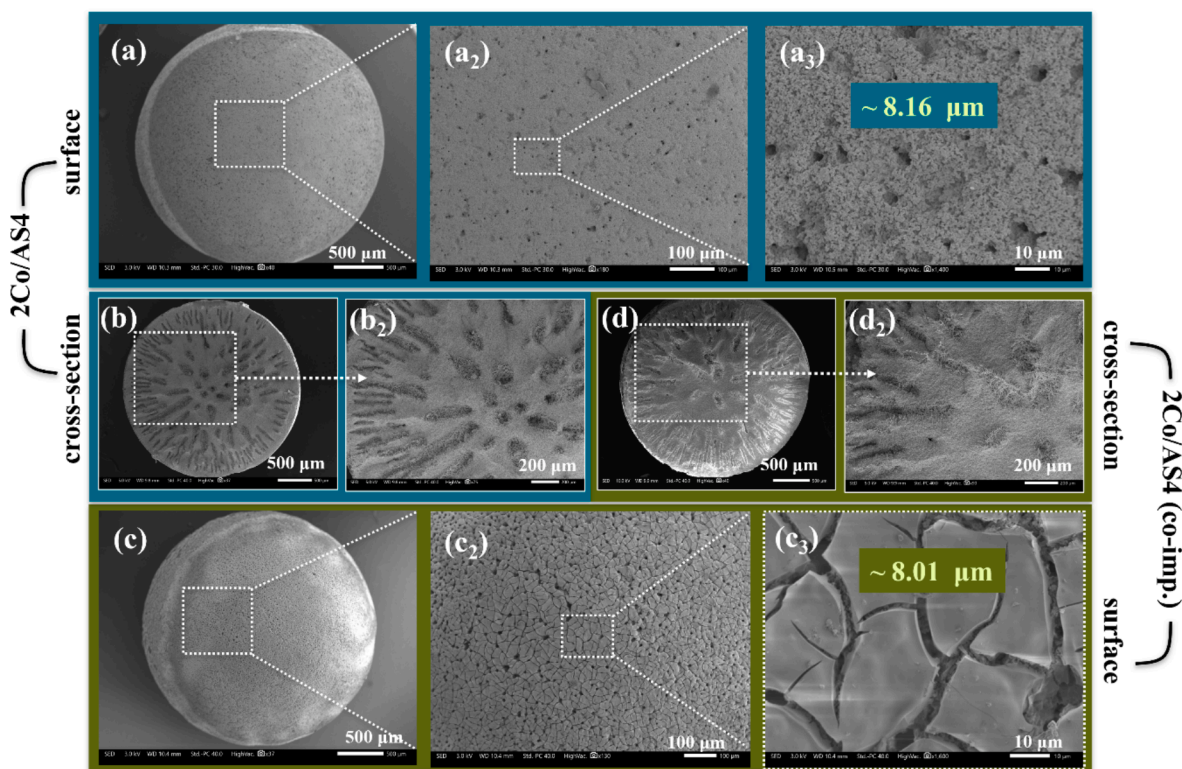
Fig.4. SEM images of (a, a_2, a_3) the surface views of 2Co/AS4, (b, b_2) cross-sectional views of 2Co/AS4, (c, c_2, c_3) the surface views of 2Co-AS4 (co-imp.), and (d, d_2) the cross-sectional views of 2Co-AS4 (co-imp.).

diffusion (e.g., open channels sizes on the bead surface) at high concentrations of organic pollutants. At higher SMX concentrations, more reactants from the bulk solution are required to diffuse into the alumina beads for the catalytic reaction, but the γ-Al_2O_3 washcoating films on the surface impaired their ability for intraparticle diffusion. Consequently, the rate constants for 2Co/AS4 and 2Co/AS4 (co-imp.) decreased from being 2.58 times and 3.72 times higher than 2Co/AS0 at 20 mg/L SMX to 1.55 times and 1.57 times higher at 40 mg/L SMX, respectively, as shown in Fig. 5 (d) and Fig. 5 (f). This is consistent with the previously published catalytic performance results, where thicker wash-coating layers led to an increase in light-off temperature, despite the large BET areas [14].

Reaction temperature is a key parameter influencing the intraparticle diffusion, as a higher temperature usually results in a faster movement of molecules. Fig. 6 revealed that at 40℃, SMX was degraded more easily under 2Co/ASx and 2Co/ASx (co-imp.) systems, in comparison to 2Co/AS0. At the beginning stage, such as 5 min, the SMX degradation efficiency (Fig. 6 (a)) reached 24.47 %, 44.69 %, 53.24 %, 58.03 %, 67.54 %, and 70.65 % for 2Co/AS0, 2Co/AS1, 2Co/AS2, 2Co/AS3, 2Co/AS4, and 2Co/AS4 (co-imp.), respectively. Similarly, Fig. 6 (c) depicted that the rate constants of 2Co/AS4 and 2Co/AS4 (co-imp.) at 5 min were 4.01 times and 4.37 times than that of 2Co/AS0. Apparently, at high reaction temperatures, the diffusion coefficient escalated, implying that the diffusion resistance for γ-Al_2O_3-loaded samples was less significant than at low temperatures; On the contrary, the surface area and dispersion of cobalt oxides had a greater impact on the catalytic performance. As the reaction continued, such as the rate constants of 120 min in Fig. 6 (d), this disparity gradually diminished because the concentration gradient of the contaminants between external and internal surfaces of the catalyst support decreased. In all reaction systems, i.e., 2Co/ASx|PMS system and 2Co/ASx (co-imp.)|PMS system, the leaching of cobalt ions was below 0.7 ppm, which was reasonable and aligned with previously published work [42].

Iqbal et al. reviewed pharmaceutical wastewater treatment using various AOPs to compare catalyst effectiveness [43]. However, in this work, a direct comparison of 2Co/ASx and 2Co/ASx (co-imp.) samples with other AOPs is challenging, as microchannel-structured alumina beads were introduced for the first time in our recent publication [10], and no other AOPs reactions involving these specific beads or commercial homogeneous beads have been reported yet. It is well-known that powdered catalysts typically exhibit higher catalytic efficiency than catalysts supported on substrates, due to limitations from diffusional mass transfer resistance, as evidenced in Fig. S6. It is also important to highlight that the molecular size of SMX is 1.49 × 0.64 × 0.56 nm [44], while the BET analysis results (Table 2) showed that the pore size of 2Co/ASx and 2Co/ASx (co-imp.) samples was approximately 10 nm, about 7 times larger than the SMX molecule. This size differential suggests that SMX molecules can efficiently enter and diffuse through the pores, effectively reaching the active sites and enhancing the SMX degradation efficiency during the AOPs reaction.

In short, all innovative microchannel-structured alumina beads after modification, whether synthesised using two-step sequential impregnation method or one-step co-impregnation method, demonstrated significantly enhanced catalytic performance for SMX abatement. As noted, this result is vital for advancing the PI technology. Although some research has explored PI at the process unit level, such as employing ceramic foam structures [6,45] and honeycomb monoliths [46,47] as catalyst supports to potentially balance mass transfer and pressure drop, it has also been reported that the external mass transfer coefficients for conventional uniform beads (1.5 mm, 3 mm), honeycombs (400 CPSI) and ceramic foams (20 pores per inch (PPI), 45 PPI) are ranked in the following order: 1.5 mm beads ≫ 45 PPI foams > 20 PPI foams ≈ 3.3 mm beads > 400 CPSI honeycombs [48]. Therefore, on the one hand, this work addressed the long-standing challenge of balancing mass transfer and pressure drop by creating innovative finger-like microchannels in beads with millimetre-scale diameter. The external mass transfer coefficient of this novel 3 mm beads (AS0) would be significantly higher than that of 3 mm conventional uniform bead, and even
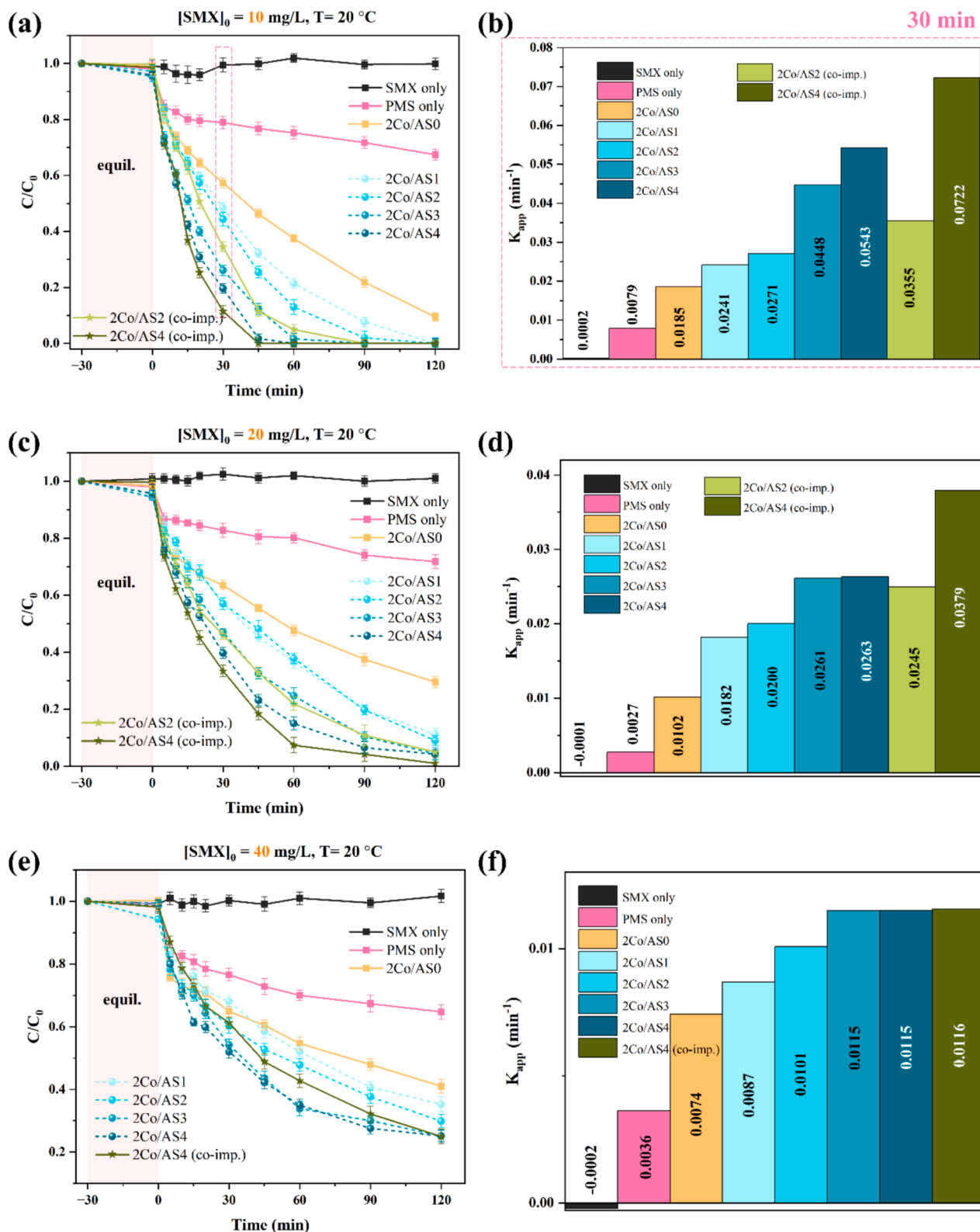
Fig.5. Degradation of different SMX concentrations at 20 ℃ and the corresponding rate constants: (a, b) $[SMX]_0$ = 10 mg/L; (c, d) $[SMX]_0$ = 20 mg/L; (e, f) $[SMX]_0$ = 40 mg/L. Reaction Conditions: $[PMS]_0$ = 0.31 mM, T = 20 ℃, $[catalyst]_0$ = 0.2 g/L, r = 150 rpm.

more so when compared to ceramic foams. On the other hand, AS*x* samples, with their increased specific surface area of the base substrates, could better disperse and deposit active components, leading to more efficient catalytic reaction simultaneously in microscale process intensification.

3.4. Possible catalytic reaction pathways and mechanism

To understand the contributions of possibly generated reactive species to the 2Co/AS4 reaction system for SMX degradation, entrapping experiments were carried out. Herein, NaN₃ (5 mM), p-benzoquinone (p-
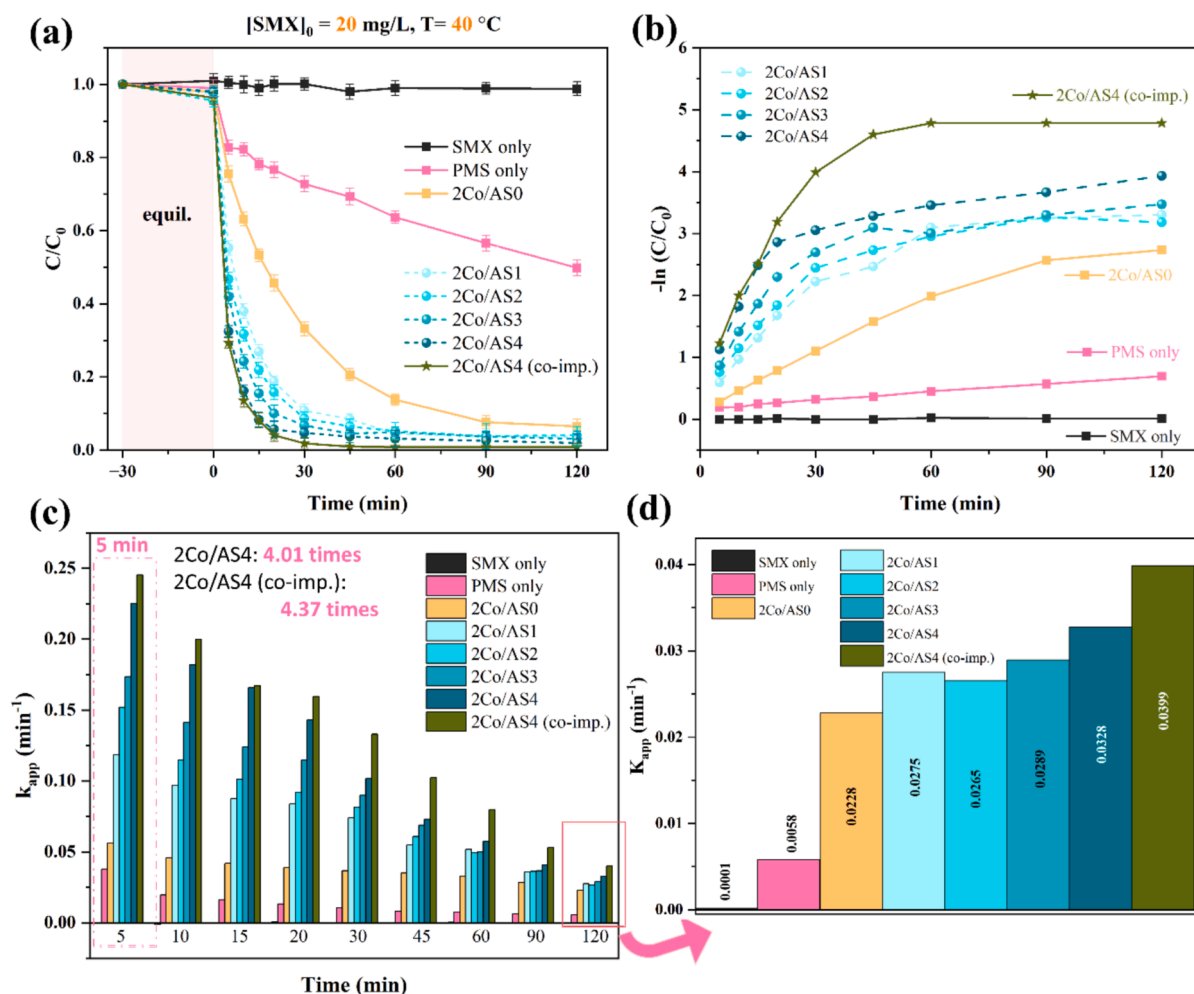
Fig.6. (a) Degradation of 20 mg/L SMX at 40 ℃, (b) their reaction kinetics, and (c, d) the corresponding rate constants. Reaction Conditions: $[PMS]_0 = 0.31$ mM, T = 20 ℃, $[catalyst]_0 = 0.2$ g/L, r = 150 rpm.

BQ, 5 mM), methanol (MeOH, 1 M) and *tert*-butanol (tBA, 1 M) were introduced into the system to capture $^1O_2$, $\cdot O_2^-$, $SO_4^{\cdot-}/\cdot OH$, and $\cdot OH$, respectively [49,50]. As shown in Fig. 7, when NaN_3 was introduced to the system, the SMX removal efficiency was significantly suppressed
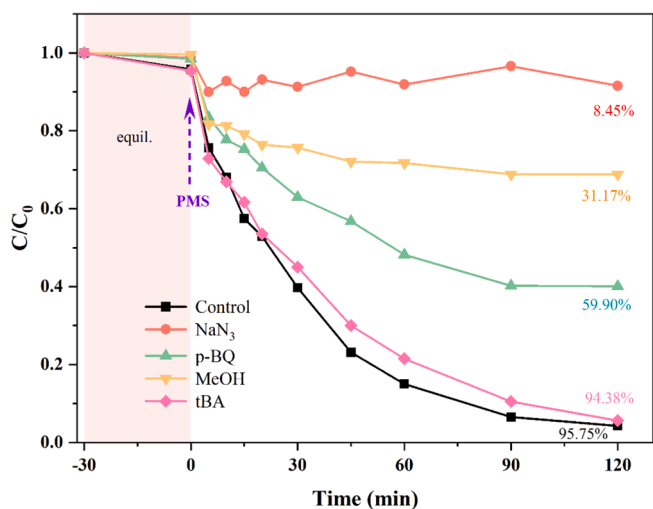
Fig.7. Effect of quenching agents on SMX degradation (catalyst: 2Co/AS4). Reaction Conditions: $[PMS]_0 = 0.31$ mM, $[SMX]_0 = 20$ mg/L, T = 20 ℃, $[catalyst]_0 = 0.2$ g/L, r = 150 rpm.

from 95.75 % to 8.45 %. Recent research revealed that two most common quenches, NaN_3 and furfuryl, could both consume either PMS or $^1O_2/\cdot OH$, affecting the removal efficiency of target contaminants [51]. Therefore, the depressed SMX degradation efficiency by adding NaN_3 may not directly reflect the dominant role of $^1O_2$ in the reaction system. Subsequent research will be conducted to explore the contribution of $^1O_2$. In contrast, the addition of p-BQ and tBA provoked the partial inhibition of 35.85 % and 1.37 % for the degradation of SMX, demonstrating a relatively minor role of $\cdot O_2^-$ and the negligible effect of $\cdot OH$, respectively. However, when MeOH was added, the degradation efficiency fell into decline rapidly (31.17 %), leading to a 64.58 % suppression of $SO_4^{\cdot-}$ and $\cdot OH$, ultimately resulting in a 63.21 % reduction in $SO_4^{\cdot-}$ alone, suggesting that $SO_4^{\cdot-}$ played a key role in the process. In this work, despite the uncertainty regarding the definite contribution of $^1O_2$, the predominant roles of $\cdot O_2^-$ and $SO_4^{\cdot-}$ were convinced, which aligns with previous studies where Co_3O_4 catalyst was applied for PMS activation [52,53].

Based on the above analysis and experimental results, a possible activation mechanism of AOPs over 2Co/AS4 for the efficient degradation of SMX was speculated in Fig. 8. In the metal oxide/PMS system, the breakdown of O-O bond in PMS (HSO_5^-) by receiving electrons from M^{n+} typically triggers the generation of $SO_4^{\cdot-}$ and $\cdot OH$, where M represents metals such as Co, Fe, Cu, etc., and n indicates different valence states [54]. When PMS was introduced, Co^{2+} on the surface of 2Co/AS4 initially activated PMS directly to generate $SO_4^{\cdot-}$ and Co^{3+} (Eq. (3)). Simultaneously, the produced Co^{3+} could react with PMS to convert

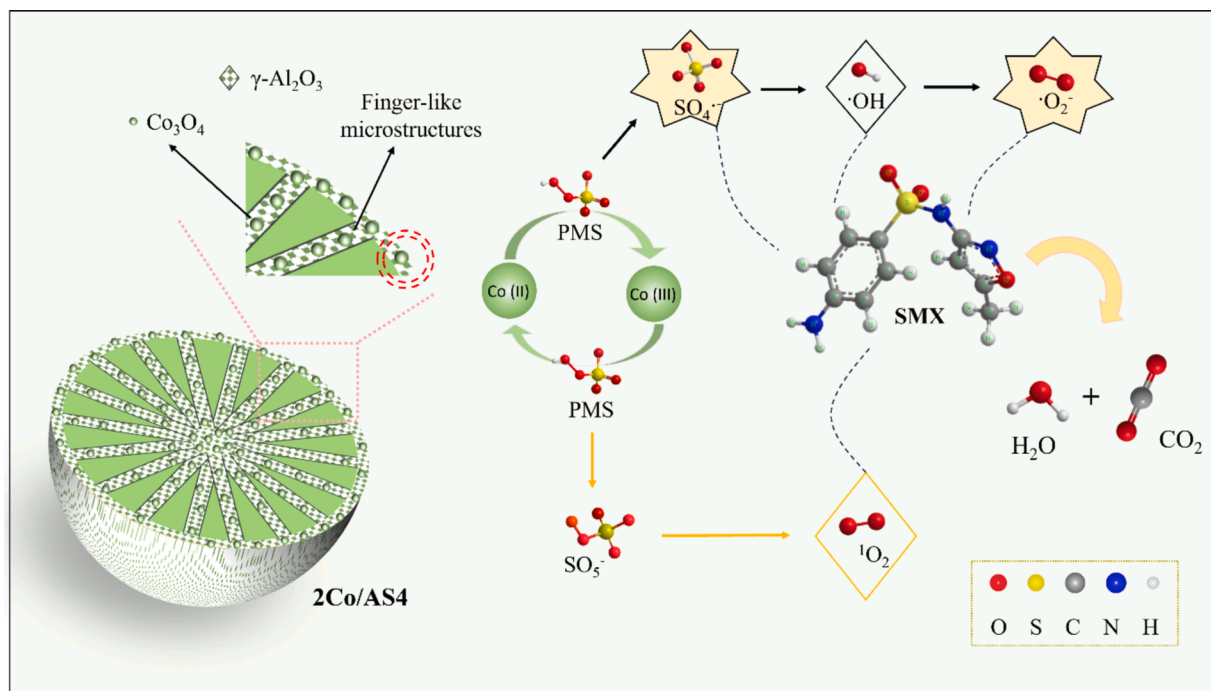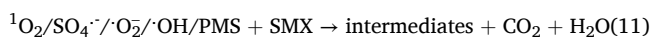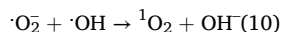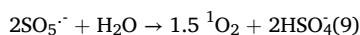**Fig.8.** A proposed mechanism for catalytic oxidation of SMX by 2Co/AS4|PMS System.

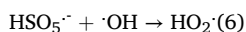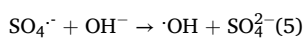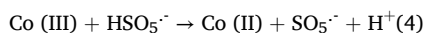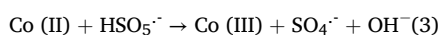back to Co^{2+}, thereby establishing a redox cycle between Co^{2+} and Co^{3+}, along with the formation of SO_5^- (Eq. (4)). This process may be accompanied by the generation of non-radical $^1O_2$ (Eq. (9)). As reaction proceed, some of the $SO_4^{\cdot-}$ radicals transformed to $\cdot OH$ (Eq. (5)) and then $\cdot O_2^-$ (Eq. (6–7)), while some $SO_4^{\cdot-}$ reacted with PMS to further be transformed to $SO_5^{\cdot-}$ (Eq. (8)), which continues to react with H_2O to form $^1O_2$ (Eq. (9)). Consequently, the primary ROS ($SO_4^{\cdot-}$) and secondary ROS ($\cdot O_2^-$, $^1O_2$) contributed to the catalytic SMX abasement by breaking it down into smaller molecules, eventually fully mineralising it into CO_2 and H_2O (Eq. (11)).

$$Co\ (II) + HSO_5^{\cdot-} \rightarrow Co\ (III) + SO_4^{\cdot-} + OH^- \quad (3)$$

$$Co\ (III) + HSO_5^{\cdot-} \rightarrow Co\ (II) + SO_5^{\cdot-} + H^+ \quad (4)$$

$$SO_4^{\cdot-} + OH^- \rightarrow \cdot OH + SO_4^{2-} \quad (5)$$

$$HSO_5^{\cdot-} + \cdot OH \rightarrow HO_2\cdot \quad (6)$$

$$HO_2\cdot \rightarrow H^+ + \cdot O_2^- \quad (7)$$

$$SO_4^{\cdot-} + HSO_5^{\cdot-} \rightarrow SO_5^{\cdot-} + HSO_4^- \quad (8)$$

$$2SO_5^{\cdot-} + H_2O \rightarrow 1.5\ ^1O_2 + 2HSO_4^- \quad (9)$$

$$\cdot O_2^- + \cdot OH \rightarrow ^1O_2 + OH^- \quad (10)$$

$$^1O_2/SO_4^{\cdot-}/\cdot O_2^-/\cdot OH/PMS + SMX \rightarrow intermediates + CO_2 + H_2O \quad (11)$$
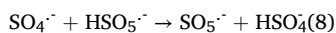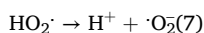
3.5. Reusability and stability of 2Co/AS4

The practical application of catalysts, particularly the microchannel-structured ceramic beads designed for industrial use in this study, also depends heavily on their reusability and stability. Herein, 2Co/AS4 was typically selected to degrade SMX for successive 16 runs. After each run, the beads were collected by simply pouring out the aqueous solution and then rinsed with deionised water. Before 5th, 9th, and 13th run, the beads were further regenerated by sintering at 450 ℃ for 1 h to remove the residue reactants and products adsorbed. As shown in Fig. 9, the sample exhibited superior reusability, with SMX removal efficiency

maintained at 95.75 %, 88.86 %, 86.07 %, and 85.17 % within 120 min for the 1st, 2nd, 3rd, and 4th run, respectively, when the sample was only reinsed with DI water. The minor reduction could be ascribed to the coverage of surface active sites by reactants and products during the degradation process, as evidenced by the SEM images in Fig. 10 (a_2, a_3). Most importantly, the regenerated sample, after being sintered, demonstrated a significantly enhanced SMX removal efficiency (100 %), even exceeding that of the fresh sample (95.75 %). This enhancement also reflected in being able to achieve a comparble removal efficiency (96.28 %) within a reaction time of just 30 min. Likewise, this phenomenon recurred during the second (9th, 100 %) and third (13th, 100 %) regenerations, whereas almost all studies have reported a downward trend due to the continuous depletion of exposed active sites and intrinsic nature of catalyst powders [49,55]. As far as we know, aside from our recent publication [10], this is the another instance where catalytic efficiency not only remained stable for reusability test but actually further improved as the cycling experiments progressed. In addition, the XRD patterns of the used samples (Fig. 9 (c)), whether used for once or 16 times, showed similar patterns without significant variation before and after reaction. This indicates the exceptional stability of the catalysts and catalyst supports throught the catalytic process. It can be concluded from the reusability and stability results that 2Co/AS*x* samples are environmentally friendly, owing to their theoretically unlimited high catalytic efficiency until complete consumption, along with the extraordinary stability and resistance to dissolution and chemical degradation of the catalyst substrates, resulting in minimal environmental impact.

In order to explore the reasons behind the improved SMX removal efficiency, Fig. 10 depicts the morphologies of the used samples at different magnifications. As illustrated in Fig. 10 (a, a_2, a_3), the surface of the used 2Co/AS4 for once was partially blocked by adsorbed reactants and products after reaction, and for other unblocked open channels, the average size was approximately 7.14 μm. The shapes of the microchannels inside in Fig. 10 (a_4, a_5) showed no obvious changes, except for a brighter colour, potentially due to the adsorbed pollutants. This is consistent with the slight decrease of catalytic SMX removal efficiency. Similarly, 2Co/AS4 used for 16th run in Fig. 10 (b, b_2, b_3) had a similar obstructed phenomenon and relatively smaller open channels
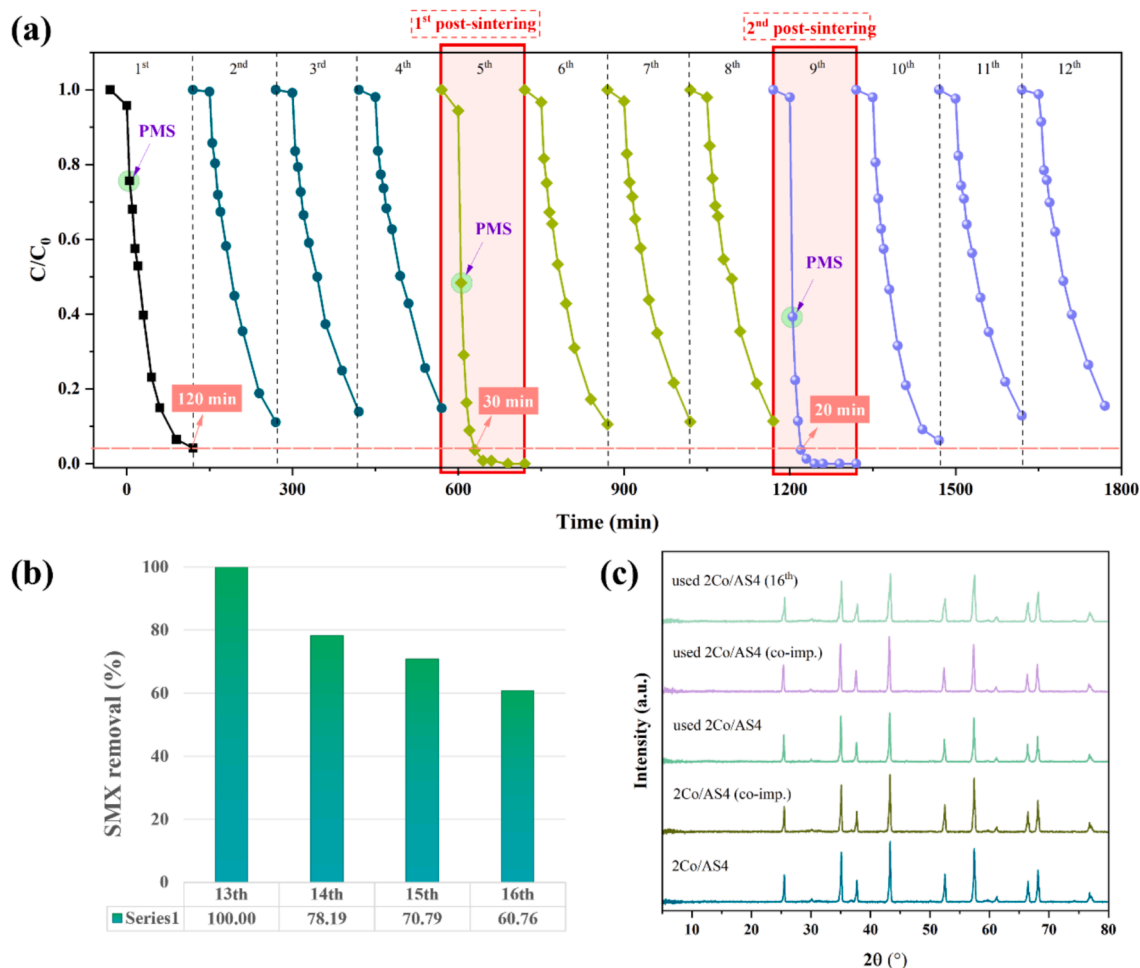
Fig.9. Reusability of the 2Co/AS4 sample on the degradation of SMX for (a, b) 16 successive cycles with being cleaned by DI water only or being regenerated by sintering at 450 ℃ for 1 h, and (c) XRD patterns of 2Co/AS4 before and after reaction.

sizes (6.99 μm). However, when the used sample 2Co/AS4 after 16th run was regenerated by post-sintering (Fig. 10 ((c, c₂, c₃)), more detectable exposed open channels could be observed, with a mean pore size of 6.77 μm. The post-sintering process facilitated the clearage of adsorbed reactants and products, which are challenging to clean with DI water. Meanwhile, the size of these open channels increased compared to the ones before (Fig. 3 (e₄, e₆), ~ 4.4 μm) and after cobalt loading (Fig. 4 (a₃), ~ 5.82 μm). This might be linked to the removal of loosely packed alumina powders from the bead surface during the post-sintering treatment, which aligns with the reusability test result for 2Co/AS0 reported in previous studies [10]. Interestingly, the size of the exposed open channels in this work after the post-sintering procedure (~ 6.77 μm) is smaller than that of 2Co/AS0 reported in the literature (~ 18 μm) [10]. This indicates that modifying AS0 with γ-Al₂O₃ sol may also enhance the stability of the catalyst supports during the catalytic reaction process, leading to reduced loss of loosely packed alumina powders. Overall, the synergistic effects of having more and larger exposed open channels in this work contributed to intraparticle diffusion, significantly enhancing the catalytic performance of SMX degradation.

4. Conclusion

In this study, microchannel-structured alumina beads (AS0, 3 mm in diameter) with enhanced S_{BET} (ASx) were prepared by phase-inversion and sol–gel methods for the first time. The improved S_{BET} was achieved by washcoating a thin layer of γ-Al₂O₃ sol onto the inner surface of

the microchannels within the alumina beads. SEM images revealed a well-defined finger-like microstructures within the alumina beads and confirmed the presence of γ-Al₂O₃ on the surface of the alumina beads and the inner walls of the microchannels inside. Afterwards, Co₃O₄ was incorporated onto the beads by two approaches: two-step sequential impregnation method (2Co/ASx) and one-step co-impregnation method (2Co/ASx (co-imp.)) for AOPs reactions. The experiment results demonstrated that the degradation efficiency of these samples improved with the rise in S_{BET} due to the increased accessible active sites. Additionally, at low γ-Al₂O₃ sol loadings, 2Co/ASx (co-imp.) exhibited higher catalytic activity compared to 2Co/ASx, which might be attributed to the high dispersion of cobalt oxide and the larger exposed open channels on the bead surface that facilitated diffusional mass transfer. Finally, it is unexpected that after being used and regenerated, 2Co/AS4 demonstrated substantially higher catalytic performance (96.32 % in 20 min) than the fresh catalyst (95.75 % in 120 min). This enhancement was consistently observed when the catalysts were regenerated by post-sintering, which could be attributed to the relatively increased number and size of exposed open channels on the surface of 2Co/AS4, which further reduced the intraparticle diffusion resistance in AOP reactions. We believe that the transferable advantages demonstrated in this work can advance the development of a broad spectrum of heterogeneous catalysis for efficient and durable catalytic reactions, including process intensification at the microscale level, benefiting both academia and industry.
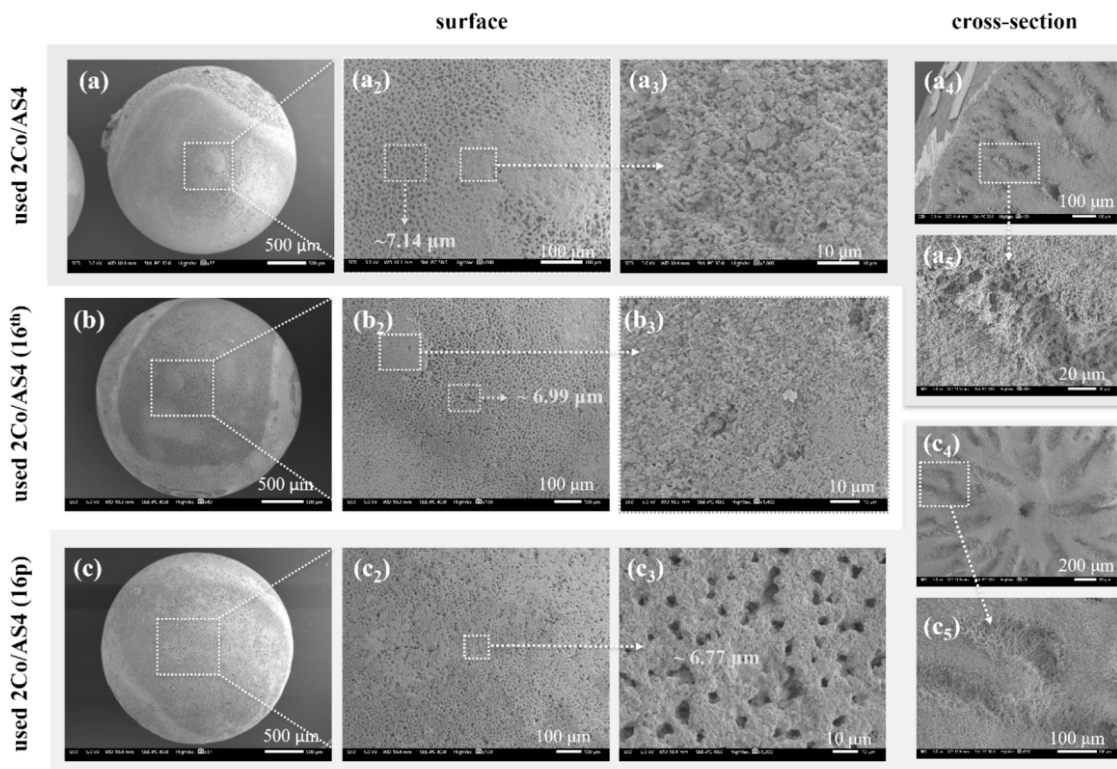
Fig.10. SEM images of (a, a₂, a₃) the surface views and (a₄, a₅) cross-sectional views of the used 2Co/AS4; (b, b₂, b₃) the surface views of the used 2Co/AS4 for 16 times; (c, c₂ , c₃) the surface views and (c₄, c₅) cross-sectional views of the used 2Co/AS4 for 16 times after regeneration.

CRediT authorship contribution statement

Jiaojiao Zheng: Writing – original draft, Validation, Methodology, Investigation, Formal analysis, Data curation. **Zhentao Wu:** Writing – review & editing, Supervision, Project administration, Funding acquisition, Conceptualization.

Declaration of competing interest

The authors declare that they have no known competing financial interests or personal relationships that could have appeared to influence the work reported in this paper.

Appendix A. Supplementary data

Supplementary data to this article can be found online at https://doi.org/10.1016/j.cej.2024.158527.

Data availability

Data will be made available on request.

References

[1] Reay, D., C. Ramshaw, and A. Harvey, *Process Intensification: Engineering for efficiency, sustainability and flexibility*. 2013: Butterworth-Heinemann.

[2] T.V.G.a.A. Stankiewicz, *Structure, energy, synergy, times the fundamentals of process intensification*, Ind. Eng. Chem. Res. 48 (5) (2009) 2465–2474.

[3] L.A. Truter, et al., *The application of palladium and zeolite incorporated chip-based microreactors*, Appl. Catal. A 515 (2016) 72–82.

[4] K.F. Jensen, *Microreaction engineering — is small better?* Chem. Eng. Sci. 56 (2) (2001) 293–303.

[5] S. LeViness, et al., *Velocys Fischer–Tropsch Synthesis Technology—New Advances on State-of-the-Art*, Top. Catal. 57 (6–9) (2013) 518–525.

[6] L. Zhang, et al., *ZSM-5@ceramic foam composite catalyst derived from spent bleaching clay for continuous pyrolysis of waste oil to produce monocyclic aromatic hydrocarbons*, Sci Total Environ 926 (2024) 171887.

[7] L. Baharudin, M.J. Watson, *Monolithic substrate support catalyst design considerations for steam methane reforming operation*, Rev. Chem. Eng. 34 (4) (2018) 481–501.

[8] J. Yue, *Green process intensification using microreactor technology for the synthesis of biobased chemicals and fuels*, Chem. Eng. Process. - Process Intesif. 177 (2022).

[9] M. Mandić, et al., *Effects of catalyst activity, particle size and shape, and process conditions on catalyst effectiveness and methane selectivity for fischer–tropsch reaction: a modeling study*, Ind. Eng. Chem. Res. 56 (10) (2017) 2733–2745.

[10] J. Zheng, et al., *Catalytic micro-structured ceramic beads and efficacy evaluation through SMX degradation in PMS-activated systems*, Sep. Purif. Technol. 354 (2025).

[11] A.I. Stankiewicz, *Process intensification: transforming Chemical Engineering*, Chem. Eng. Prog. 96 (2000) 22–34.

[12] H.A. Ibrahim, et al., *Experimental and numerical investigations of flow through catalytic converters*, Int. J. Heat Mass Transf. 127 (2018) 546–560.

[13] Q. Zuo, et al., *NO catalytic performance analysis of gasoline engine tapered variable cell density carrier catalytic converter*, Environ. Sci. Pollut. Res. Int. 29 (1) (2022) 1413–1429.

[14] N.I. Mahyon, et al., *A new hollow fibre catalytic converter design for sustainable automotive emissions control*, Catal. Commun. 120 (2019) 86–90.

[15] J.A. Moulijn, et al., *Process intensification and process systems engineering: A friendly symbiosis*, Comput. Chem. Eng. 32 (1–2) (2008) 3–11.

[16] X. Liu, et al., *Investigation of spherical alumina supported catalyst for carbon nanotubes production from waste polyethylene*, Process Saf. Environ. Prot. 146 (2021) 201–207.

[17] H.V. Fajardo, L.F.D. Probst, *Production of hydrogen by steam reforming of ethanol over Ni/Al2O3 spherical catalysts*, Appl. Catal. A 306 (2006) 134–141.

[18] J. Howeizi, et al., *Effect of the distribution and dispersion of palladium nanoparticles on the reducibility and performance of Pd/Al2O3 catalyst in liquid-phase hydrogenation of olefins*, React. Kinet. Mech. Catal. 130 (2) (2020) 777–795.

[19] J. Wärnå, et al., *Influence of intraparticle reaction–diffusion in a catalytic reactor*, Chem. Eng. J. 90 (1) (2002) 209–212.

[20] S. Afandizadeh, E.A. Foumeny, *Design of packed bed reactors: guides to catalyst shape, size, and loading selection*, Appl. Therm. Eng. 21 (6) (2001) 669–682.

[21] F. Chen, et al., *High-loading washcoat of γ-alumina on FeCrAlloy mesh with acid-free slurry*, Surf. Coat. Technol. 403 (2020).

[22] D. Lin, et al., *Application of persulfate-based oxidation processes to address diverse sustainability challenges: a critical review*, J Hazard Mater 440 (2022) 129722.

[23] H. Liu, et al., *Ball milling treatment of Mn₃O₄ regulates electron transfer pathway for peroxymonosulfate activation*, Chem. Eng. J. 467 (2023).

[24] H. Liu, et al., *Mechanochemically synthesized Mn₃O₄@β-cyclodextrin mediates efficient electron transfer process for peroxymonosulfate activation*, Sep. Purif. Technol. 326 (2023).

[25] G. Ruhi, et al., *Effect of sintering temperatures on corrosion and wear properties of sol–gel alumina coatings on surface pre-treated mild steel*, Corros. Sci. 50 (3) (2008) 639–649.

[26] H. Koopi, F. Buazar, *A novel one-pot biosynthesis of pure alpha aluminum oxide nanoparticles using the macroalgae Sargassum ilicifolium: a green marine approach*, Ceram. Int. 44 (8) (2018) 8940–8945.

[27] S.-H. Lai, et al., *Novel g-C3N4 wrapped γ-Al₂O₃ microspheres heterojunction for efficient photocatalytic application under visible light irradiation*, J. Mater. Sci. Mater. Electron. 29 (6) (2017) 4509–4516.

[28] Q. Guo, et al., *Effect of lanthanum on Zr–Co/γ-Al₂O₃ catalysts for Fischer–Tropsch synthesis*, Catal. Lett. 148 (9) (2018) 2789–2798.

[29] L. He, et al., *Preparation of Pt/γ-Al₂O₃ catalyst coating in microreactors for catalytic methane combustion*, Chem. Eng. J. 380 (2020).

[30] I.B. Singh, O.P. Modi, G. Ruhi, *Development of sol–gel alumina coating on 9Cr–1Mo ferritic steel and their oxidation behavior at high temperature*, J. Sol-Gel Sci. Technol. 74 (3) (2015) 685–691.

[31] A. Irankhah, et al., *Fischer-Tropsch reaction kinetics of cobalt catalyst in supercritical phase*, J. Nat. Gas Chem. 16 (2) (2007) 115–120.

[32] R. Gheitanchi, et al., *Effects of ceria addition and pre-calcination temperature on performance of cobalt catalysts for Fischer-Tropsch synthesis*, React. Kinet. Catal. Lett. 88 (2) (2006) 225–232.

[33] N. Zhao, et al., *Preparation of high performance Co₃O₄/Al₂O₃ catalysts by doping Al into ZIF-67: effect of Al sources on Fischer-Tropsch synthesis*, Appl. Surf. Sci. 570 (2021).

[34] S. Guo, et al., *Effect of Ba on the catalytic performance of Co-Ru/Al2O3 catalyst for Fischer-Tropsch synthesis*, Fuel 292 (2021).

[35] C. Agrafiotis, A. Tsetsekou, *The effect of processing parameters on the properties of γ-alumina washcoats deposited on ceramic honeycombs*, J. Mater. Sci. 35 (4) (2000) 951–960.

[36] J. Zheng, et al., *A visible-light-driven heterojuncted composite WO3/Bi12O17Cl2: synthesis, characterization, and improved photocatalytic performance*, J. Colloid Interface Sci. 510 (2018) 20–31.

[37] J.P. Zou, et al., *Electrochemical oxidation and advanced oxidation processes using a 3D hexagonal Co(3)O(4) array anode for 4-nitrophenol decomposition coupled with simultaneous CO(2) conversion to liquid fuels via a flower-like CuO cathode*, Water Res 150 (2019) 330–339.

[38] Q. Guo, et al., *Co(3)O(4) modified polymeric carbon nitride for external light-free chlorine activating degradation of organic pollutants*, J Hazard Mater 429 (2022) 128193.

[39] T. Song, et al., *Fabrication of super slippery sheet-layered and porous anodic aluminium oxide surfaces and its anticorrosion property*, Appl. Surf. Sci. 355 (2015) 495–501.

[40] T. Tago, et al., *XPS study from a clean surface of Al₂O₃ single crystals*, Procedia Eng. 216 (2017) 175–181.

[41] Zhou, X., et al., Atomic cation-vacancy modulated peroxymonosulfate nonradical oxidation of sulfamethoxazole via high-valent iron-oxo species. Appl. Catal. B: Environ., 2023. **330**.

[42] A.H. Asif, et al., *Heterogeneous activation of peroxymonosulfate by Co-doped Fe(2)O(3) nanospheres for degradation of p-hydroxybenzoic acid*, J. Colloid Interface Sci. 604 (2021) 390–401.

[43] J. Iqbal, et al., *Pharmaceuticals wastewater treatment via different advanced oxidation processes: reaction mechanism, operational factors, toxicities, and cost evaluation – a review*, Sep. Purif. Technol. 347 (2024).

[44] R. Mu, et al., *Functionally-designed metal salt and ball milling co-modified sludge biochar for adsorptive removal of trace level sulfamethoxazole: behavior, characterization, mechanism and DFT study*, J. Environ. Chem. Eng. 12 (5) (2024).

[45] L. Giani, G. Groppi, E. Tronconi, *Mass-transfer characterization of metallic foams as supports for structured catalysts*, Ind. Eng. Chem. Res. 44 (14) (2005) 4993–5002.

[46] M. Parsa, et al., *Regenerable carbon honeycomb monoliths directly prepared from brown coal: a novel carbon product*, Chem. Eng. J. 471 (2023).

[47] G. Vega, et al., *3D honeycomb monoliths with interconnected channels for the sustainable production of dihydroxybenzenes: towards the intensification of selective oxidation processes*, Chem. Eng. Process. - Process Intesif. 165 (2021).

[48] F.C. Patcas, G.I. Garrido, B. Kraushaar-Czarnetzki, *CO oxidation over structured carriers: a comparison of ceramic foams, honeycombs and beads*, Chem. Eng. Sci. 62 (15) (2007) 3984–3990.

[49] R.A.K. Hirani, et al., *Heterogeneous activation of persulfate by macroscopic nitrogen-doped graphene oxide cubes for the degradation of antibiotic contaminants in water*, Sep. Purif. Technol. 319 (2023) 124110.

[50] R. Wang, et al., *Non-radical mediated reduced graphene oxide/polypyrrole catalytic ceramic membrane-PDS system for source control of SMX*, Chem. Eng. J. 479 (2024) 147769.

[51] S. Wang, J. Wang, *Radiation-induced preparation of nanoscale CoO@graphene oxide for activating peroxymonosulfate to degrade emerging organic pollutants*, Sci. Total Environ. 933 (2024) 173211.

[52] Y. Liu, et al., *Regulating the Co 3d center of Co₃O₄ by Co₃O₄/g-C₃N₄ to enhance electronic activity for sulfamethizole effectively degaradtion by permonosulfate activation*, Chem. Eng. J. 489 (2024).

[53] P. Li, et al., Defect-engineered Co3O4 with porous multishelled hollow architecture enables boosted advanced oxidation processes. Appl. Catal. B: Environ., 2021. **298**.

[54] C. Yu, et al., *Marriage of membrane filtration and sulfate radical-advanced oxidation processes (SR-AOPs) for water purification: Current developments, challenges and prospects*, Chem. Eng. J. 433 (2022).

[55] M. Xiong, et al., *Efficient peroxymonosulfate activation by magnetic CoFe₂O₄ nanoparticle immobilized on biochar toward sulfamethoxazole degradation: performance, mechanism and pathway*, Appl. Surf. Sci. 615 (2023) 156398.